

Upgrading the GRAVITY fringe tracker for GRAVITY+

Tracking the white light fringe in the non-observable Optical Path Length state-space

M. Nowak^{1,2*}, S. Lacour^{3,4*}, R. Abuter⁴, J. Woillez⁴, R. Dembet³, M. S. Bordoni⁵, G. Bourdarot⁵, B. Courtney-Barré^{4,6}, D. Defrère¹⁰, A. Drescher⁵, F. Eisenhauer⁵, M. Fabricius⁵, H. Feuchtgruber⁵, R. Frahm⁴, P. Garcia^{13,14}, S. Gillessen⁵, V. Gopinath⁵, J. Graf⁵, S. Hoenig⁷, L. Kreidberg⁸, R. Laugier¹⁰, J.B. Le Bouquin⁹, D. Lutz⁵, F. Mang⁵, F. Millour¹¹, N. More⁵, N. Morujão^{13,14}, T. Ott⁵, T. Paumard³, G. Perrin³, C. Rau⁵, D. C. Ribeiro⁵, J. Shangguan⁵, T. Shimizu⁵, F. Soulez¹², C. Straubmeier¹⁵, F. Widmann⁵, and B. Wolff⁴

(Affiliations can be found after the references)

February 7, 2024

ABSTRACT

Context. Over the recent years, the GRAVITY beam-combiner at the Very Large Telescope Interferometer has made important contributions to many different fields of astronomy, from observations of the Galactic centre to the study of massive stars, young stellar objects, exoplanet atmospheres, and active galactic nuclei. Getting to this point where optical interferometry is playing a pivotal role in astronomy was only made possible by the development of several key technologies. Among these, the development of a reliable and high-performance fringe tracker stands out. These systems compensate for disturbances ranging from atmospheric turbulence to vibrations in the optical system, enabling long exposures and ensuring the stability of interferometric measurements.

Aims. As part of the ongoing GRAVITY+ upgrade of the Very Large Telescope Interferometer infrastructure, we aim to improve the performance of the GRAVITY Fringe-Tracker, and to enable its use by other instruments.

Methods. We modify the group delay controller to consistently maintain tracking in the white light fringe, characterised by a minimum group delay. Additionally, we introduce a novel approach in which fringe-tracking is performed in the non-observable Optical Path Length state-space, using a covariance-weighted Kalman filter and an auto-regressive model of the disturbance. We outline this new state-space representation, and the formalism we use to propagate the state-vector and generate the control signal. While our approach is presented specifically in the context of GRAVITY/GRAVITY+, it can easily be adapted to other instruments or interferometric facilities.

Results. We successfully demonstrate phase delay tracking within a single fringe, with any spurious phase jumps detected and corrected in less than 100 ms. We also report a significant performance improvement, as evidenced by a reduction of ~ 30 to 40% in phase residuals, and a much better behaviour under sub-optimal atmospheric conditions. Compared to what was observed in 2019, the median residuals have decreased from 150 nm to 100 nm on the Auxiliary Telescopes and from 250 nm to 150 nm on the Unit Telescopes.

Conclusions. The improved phase-delay tracking combined with white light fringe tracking means that from now-on, the GRAVITY Fringe-Tracker can be used by other instruments operating in different wavebands. The only limitation remains the need for an optical path dispersion adjustment.

Key words. Instrumentation: interferometers – Techniques: high angular resolution

1. Introduction

By combining the light from multiple telescopes, long-baseline optical interferometry can achieve angular-resolution much higher than what is possible with a single-dish telescope. Even in the upcoming era of 30+m class telescope, the Very Large Telescope Interferometer (VLTI) will continue to outperform single-dish observations in terms of angular resolution (for an up-to-date overview, see Eisenhauer et al. 2023). This is particularly useful for many applications, as evidenced by the broad range of subjects to which it has been applied with groundbreaking results (GRAVITY Collaboration et al. 2018a,b,c, 2019a,b,c, 2020a,b,c,d,e,f, 2021, 2022).

One of the challenges which arise at such high angular resolution is the need to manage disturbances which can include atmospheric turbulence, telescope vibrations, and other noise sources, and which remain the primary limitations to the precision of interferometric measurements. Such disturbances lead

to variations in the Optical Path Length (OPL) of light travelling through each telescope to the beam combiner, resulting in an unstable interference pattern (unstable "fringes").

To obtain stable interferometric measurements, these fringes need to be controlled in real-time, and any OPL fluctuations need to be compensated for. In modern instruments, this is the role of a specific subsystem: the Fringe-Tracker (FT). The crucial role of Fringe-Tracking in optical interferometry has justified the extensive development efforts made over the past decades (Shao et al. 1988; Sorrente et al. 2001; Delplancke et al. 2006; Le Bouquin et al. 2008; Cassaing et al. 2008; Houairi et al. 2008; Colavita et al. 2010; Lozi et al. 2011; Menu et al. 2012; Choquet et al. 2014; Lacour et al. 2019). Various techniques have been proposed, either based on hardware or software solutions, but they all share a common objective: to measure and stabilise the fringes, thereby maximising the Signal-to-Noise Ratio (SNR) of interferometric measurements.

For the GRAVITY instrument, the fringe-tracker was initially designed to perform control in the 6-dimensional Optical

* These authors contributed equally.

Path Delay (OPD) state-space, where measurements are available. The algorithm, described in Lacour et al. (2019) (subsequently Paper I), was based around the use of an Auto-Regressive (AR) model to model the disturbance in OPD space, and a Kalman filter to propagate an OPD state-vector using an asymptotic approximation of the optimal gain.

Deviating from this initial concept, we hereafter introduce a novel approach in which fringe-tracking is performed in the 4-dimensional non-observable OPL state-space. The reduction in dimensionality alleviates the need for an asymptotic approximation of the Kalman gain, whose optimal value is now dynamically calculated at each iteration. This work is part of a general upgrade of the GRAVITY Fringe-Tracker which happened in late 2022 and 2023, and can be seen as a follow-up to Paper 1.

The paper is divided as follows. Section 2 gives a general description of how measurements are made within the FT, and which quantities are observable. Section 3 describes the details of the implementation of the upgraded FT, and in particular the state-space model, and the two control loops (phase and group-delay). Section 4 reports on the first on-sky results obtained with this upgraded FT, with an emphasis on the behaviour of the group-delay control loop. Finally, Section 5 gives some prospects and avenues for future work, and Section 6 gives our final conclusions.

2. Observables

2.1. From pixels to fluxes

In GRAVITY, the fringe tracking beam combiner, like the science combiner, is a silica-on-silicium integrated optics component, which uses an ABCD beam-combining scheme. This means that for any given baseline j, k linking telescopes T_j to T_k , the beam-combiner registers a set of four outputs, corresponding to four values of additional phase shifts introduced between the beams ($0, \pi/2, \pi$, and $3\pi/2$):

$$a_{j,k} = \langle |E_j|^2 + |E_k|^2 + 2\text{Re}(E_j E_k^*) \rangle, \quad (1)$$

$$b_{j,k} = \langle |E_j|^2 + |E_k|^2 + 2\text{Re}(E_j E_k^* e^{i\pi/2}) \rangle, \quad (2)$$

$$c_{j,k} = \langle |E_j|^2 + |E_k|^2 + 2\text{Re}(E_j E_k^* e^{i\pi}) \rangle, \quad (3)$$

$$d_{j,k} = \langle |E_j|^2 + |E_k|^2 + 2\text{Re}(E_j E_k^* e^{3\pi/2}) \rangle, \quad (4)$$

where E is the complex amplitude of the electric field at the input of the combiner, $\langle \cdot \rangle$ denotes the average over the integration time, and $*$ the complex conjugate.

In principle, both the coherent flux $\Gamma_{j,k} = \langle E_j E_k^* \rangle$ and the incoherent flux $F_j + F_k = \langle |E_j|^2 \rangle + \langle |E_k|^2 \rangle$ can be recovered by linear combinations of these 4 outputs:

$$F_j + F_k = (a_{j,k} + b_{j,k} + c_{j,k} + d_{j,k})/4, \quad (5)$$

$$\Gamma_{j,k} = (a_{j,k} - c_{j,k})/2 + i(d_{j,k} - b_{j,k})/2. \quad (6)$$

And each individual F_j for $j \in [1 \dots 4]$ can subsequently be recovered by a second linear combination of the different baselines:

$$F_j = \sum_{k \neq j} (F_j + F_k)/3 - \sum_{\substack{k, l \neq j \\ k < l}} (F_k + F_l)/6. \quad (7)$$

In the GRAVITY FT, the 24 outputs (4 outputs per each of the 6 ABCD combiners) are dispersed over 6 wavelength channels in the K-band, and recorded on a SAPHIRA detector (Finger

et al. 2014). We refer to Figure 1 in Paper 1 for an overview of the pixel arrangement on the detector Real Time Display (RTD). As shown by Equations 1 to 7, for a given wavelength channel, the column vector $(q_1, \dots, q_{24})^T$ containing the 24 different intensity outputs and the column-vector $(F_j, \Gamma_{j,k})^T$ containing the 10 incoherent and coherent flux values are related by a multiplication by a single matrix: the P2VM (Pixel to Visibility Matrix):

$$\text{P2VM} \cdot (q_1, \dots, q_{24})^T = (F_1, \dots, F_4, \Gamma_{1,2}, \dots, \Gamma_{3,4})^T. \quad (8)$$

The incoherent and coherent fluxes are computed in real time for each of the wavelength channels, which are treated independently. Similarly, if polarisation is split, the two polarisation are treated independently.

In practice, the ABCD combiners are not perfectly balanced, and the phase offsets can be different from their fiducial values, which means that the coefficients linking the ABCD outputs to the complex amplitudes of the electric field in Equations 1 to 4 can vary. Therefore, the P2VM must be calibrated, which in GRAVITY is done during daytime using an internal source. This P2VM formalism was initially introduced by Tatulli et al. (2007) for the AMBER instrument (Petrov et al. 2007). It was then adapted to ABCD combiners by Lacour et al. (2008), and more details on its implementation can be found in these papers, along with Paper 1.

2.2. From fluxes to phase/group delays and closures

After the P2VM calculation, the resulting wavelength dependent coherent fluxes $\Gamma_{j,k,\lambda}$ are still affected by dispersion (both atmospheric dispersion, and dispersion in the fibre delay lines, FDDL), which at first order introduces a phase curvature of the form $e^{iD(1-\lambda_0/\lambda)^2}$, where $\lambda_0 = 2.2 \mu\text{m}$. This is corrected by using an empirical value for D , which depends on the position of the star in the sky, and on the position of the FDDLs. This correction was calibrated during the first year of on-sky observations.

From this dispersion-corrected coherent flux measurement, we calculate the OPD for each baseline, denoted $\phi_{j,k}$, using:

$$\phi_{j,k} = \frac{\lambda_0}{2\pi} \times \arg \left(\sum_{\lambda=1}^{N_\lambda} \Gamma_{j,k,\lambda} \right). \quad (9)$$

These values are concatenated to form the OPD vector Φ , using the convention: $\Phi = (\phi_{21}, \phi_{31}, \phi_{41}, \phi_{32}, \phi_{42}, \phi_{43})^T$. The closure phase $\theta_{j,k,l}^{\text{PD}}$ over the triangle linking telescopes T_j, T_k and T_l is calculated in unit of length using:

$$\theta_{j,k,l}^{\text{PD}} = \frac{\lambda_0}{2\pi} \times \arg \left(\left\langle \left(\sum_{\lambda=1}^{N_\lambda} \Gamma_{j,k,\lambda} \sum_{\lambda=1}^{N_\lambda} \Gamma_{k,l,\lambda} \sum_{\lambda=1}^{N_\lambda} \Gamma_{j,l,\lambda}^* \right) \right\rangle_{350\text{DITs}} \right), \quad (10)$$

where the incoherent flux is first averaged over 350 Detector Integration Times (DITs, i.e. bout 385 ms at 909 Hz) to boost signal-to-noise, the phase closure being a notoriously noisy quantity.

To calculate the group delay $\psi_{j,k}$ and group closure $\theta_{j,k,l}^{\text{GD}}$, we first correct the coherent flux for any phase offset constant in wavelength by subtracting the phase delay, and we then average it over 150 DITs (about 165 ms at 909 Hz), again to boost signal-to-noise ratio:

$$\Gamma'_{j,k,\lambda} = \left\langle \Gamma_{j,k,\lambda} \exp \left[-i \frac{2\pi}{\lambda_0} \phi_{j,k} \right] \right\rangle_{150\text{DITs}}. \quad (11)$$

The group delay is then given by:

$$\psi_{j,k} = \frac{\Delta\lambda}{2\pi} \times \arg \left(\sum_{\lambda=1}^{N_{\lambda}-1} \Gamma'_{j,k,\lambda+1} \Gamma'^{*}_{j,k,\lambda} \right), \quad (12)$$

where $\Delta\lambda$ is the difference between the effective wavelength of two pixel bins. From this, we also construct another vector in OPD-space: $\Psi = (\psi_{21}, \psi_{31}, \psi_{41}, \psi_{32}, \psi_{42}, \psi_{43})^T$. The closure of the group delay can be written as:

$$\theta_{j,k,l}^{\text{GD}} = \frac{\Delta\lambda}{2\pi} \times \arg \left(\left\langle \sum_{\lambda=1}^{N_{\lambda}-1} \Gamma'_{j,k,\lambda+1} \Gamma'^{*}_{j,k,\lambda} \sum_{\lambda=1}^{N_{\lambda}-1} \Gamma'_{k,l,\lambda+1} \Gamma'^{*}_{k,l,\lambda} \sum_{\lambda=1}^{N_{\lambda}-1} \Gamma'_{j,l,\lambda+1} \Gamma'^{*}_{j,l,\lambda} \right\rangle_{350 \text{ DITs}} \right). \quad (13)$$

The last quantity of interest for the control algorithm is the uncertainty on the estimation of the OPD, $\sigma_{j,k}$. This uncertainty can be computed by first introducing the interferometric SNR, defined as the ratio between the modulus of the coherent flux and the square-root of its variance. We approximate this variance as the half sum of the variance of the real and imaginary parts of the coherent flux, and we average the SNR over 3 DITs¹:

$$\text{SNR}_{j,k} = \left\langle \frac{|\sum_{\lambda} \Gamma_{j,k,\lambda}|}{\sqrt{\frac{1}{2} \sum_{\lambda} \text{Var}(\Re \Gamma_{j,k,\lambda}) + \frac{1}{2} \sum_{\lambda} \text{Var}(\Im \Gamma_{j,k,\lambda})}} \right\rangle_{3 \text{ DITs}}. \quad (14)$$

The uncertainty on the phase can then be computed using a similar approach as in the Appendix of Shao et al. (1988):

$$\frac{1}{\sigma_{j,k}} = \frac{2\pi}{\lambda_0} \times \text{SNR}_{j,k}. \quad (15)$$

In Equation 14, the variance of the real and imaginary parts of the coherent flux are estimated for each frame from the background, detector and photon noises. Using these OPD noise estimators, and under the assumption that each baseline noise is uncorrelated, we also write the covariance matrix W on Φ :

$$W = \text{diag}(\sigma_{21}^2, \sigma_{31}^2, \sigma_{41}^2, \sigma_{32}^2, \sigma_{42}^2, \sigma_{43}^2). \quad (16)$$

The variance of Γ is estimated from the variance on the individual pixels q_j , multiplied by the P2VM and P2VM^T matrix, as described in Section 3.4 of Paper 1. Compared to Paper 1, where the $\sigma_{j,k}$ were computed coherently on 5 DITs, the new uncertainties are now computed on individual DITs, and then averaged only over 3 DITs. This change is motivated by the use of an adaptive gain in the new control algorithm, which strongly benefits from a better estimate of the instantaneous signal-to-noise ratio.

3. Control loop

3.1. The 3 challenges of building a fringe tracker

A first challenge that need to be solved in the implementation of a fringe tracker is that it the dichotomy between two distinct spaces. The FT uses a set of four piezoelectric delay lines (Pfuhl et al. 2014) to change the OPL of the 4 beams (one per telescope). But the feedback is provided by measurements of the coherent fluxes (see Section 2), which are transformed in a set

¹ We thank the referee for pointing out that calculating this SNR as the ratio between the average of the numerator and the average of the denominator (as opposed to the average of the ratio) would likely result in a better estimate. We plan on testing this and implementing it in a future version of the FT.

of 6 measurements of OPD ϕ (one per baseline) and group delay ψ . The OPL space itself is not observable, and this mismatch between the control space and the measurement space creates a paradox which needs to be solved by the system.

A second challenge arises from the need to regularly update the model used to represent and predict the disturbance. To do so, we use a set of AR models, whose parameters are updated every few seconds via a model fitting routine performed on a separate computer (see hardware description in section 4.1). But in order to perform the model fitting, this computer needs to be fed with measurements that represents the disturbance only, excluding the additional piezo command. The control must therefore work with a state model which explicitly separates the OPL in two components: a disturbance component L which represents both atmospheric and “mechanical” turbulence, and the OPL introduced by the piezo actuators X . Of course, only the total OPD, which derives from the total OPL $L + X$, is actually observable by the fringe-tracker. But in order to be able to update the disturbance model, the two components must be kept separated.

A third challenge comes from the fact that the main phase control loop is fed by phase measurements, which are only known to a modulo 2π (or λ_0 , in terms of OPD). Thus, this loop is blind to any potential “fringe shift”, which is the reason why we need the additional group delay loop. In Paper 1, the controller consisted of two completely independent loops running in parallel, with the potential to issue conflicting commands. The algorithm developed at the time did ensure that the integrator of the two controllers would not diverge too widely, but it did not strictly constrain the absolute group delay. The consequence was a tendency of the fringe tracker to jump between fringes during a single observation. The updated architecture detailed in this work provides a much more unified approach to controlling both the group and phase delays, thereby avoiding conflicting commands, mitigating phase jumps and maintaining tracking of the white light fringe.

3.2. State model

To solve these challenges, we adopt a state model in OPL space which explicitly separates the disturbance and the OPL introduced by the actuators. We use a set of two state vectors, which both have the unit of length, and which we denote X_n and L_n . For simplicity, these state-vectors can be broken down into four independent vectors, corresponding to each telescope. For a given telescope T_k , the vector of the last N values of OPL introduced respectively by the piezo actuators ($X_{n,k}$) and by the disturbance ($L_{n,k}$) can be expressed by:

$$X_{n,k} = [x_k(t_n), x_k(t_{n-1}), \dots, x_k(t_{n-N+1})]^T, \quad (17)$$

$$L_{n,k} = [l_k(t_n), l_k(t_{n-1}), \dots, l_k(t_{n-N+1})]^T, \quad (18)$$

where $x_k(t_j)$ and $l_k(t_j)$ respectively denotes the OPL introduced by the piezo actuator and disturbance on telescope T_k at time t_j . These vectors have a total length of 150, which matches the smoothing length of the group delay. The four telescopes can be concatenated to give our two final state vectors X_n and L_n of dimension $4 \times 150 = 600$:

$$X_n = \begin{bmatrix} X_{n,1} \\ X_{n,2} \\ X_{n,3} \\ X_{n,4} \end{bmatrix} \quad L_n = \begin{bmatrix} L_{n,1} \\ L_{n,2} \\ L_{n,3} \\ L_{n,4} \end{bmatrix} \quad (19)$$

Each of the piezo control chain (which include the actuator response as well as the pure delay introduced by the processing)

has a response function which we model as a fifth-order, where the position of the piezo at time t_n is derived from the command sent at the last five time steps:

$$x_k(t_{n+1}) = c_{k,0}u_k(t_n) + c_{k,1}u_k(t_{n-1}) + \dots + c_{k,4}u_k(t_{n-4}) \quad (20)$$

The c coefficients can be empirically measured by sending an impulse command (in Volts) through the control chain and measuring how the response evolves with time (Figure 1).

We then introduce the command vectors $U_{n,k} = [u_k(t_n), \dots, u_k(t_{n-4})]$ such that:

$$x_k(t_{n+1}) = [c_{k,0} \ c_{k,1} \ c_{k,2} \ c_{k,3} \ c_{k,4}] \cdot U_{n,k}. \quad (21)$$

Again, the four telescopes can be concatenated to give U_n of dimension $4 \times 5 = 20$:

$$U_n = \begin{bmatrix} U_{n,1} \\ U_{n,2} \\ U_{n,3} \\ U_{n,4} \end{bmatrix}. \quad (22)$$

With these notations, the propagation of the piezo state vector X_n takes the form:

$$X_{n+1} = A_X \cdot X_n + C \cdot U_n, \quad (23)$$

where A_X is a 600×600 block-diagonal matrix that just “shifts” the x s for each telescope:

$$A_X = \text{diag}(A, A, A, A), \quad (24)$$

with

$$A = \begin{bmatrix} 0 & 0 & \dots & 0 & 0 \\ 1 & 0 & \dots & 0 & 0 \\ 0 & 1 & \ddots & \vdots & \vdots \\ \vdots & \ddots & \ddots & 0 & 0 \\ 0 & \dots & 0 & 1 & 0 \end{bmatrix}, \quad (25)$$

and C is also a block-diagonal matrix, but of size 600×20 , which contains the coefficients of the piezo responses:

$$C = \text{diag}(C_1, C_2, C_3, C_4), \quad (26)$$

with

$$C_k = \begin{bmatrix} c_{k,0} & c_{k,1} & c_{k,2} & c_{k,3} & c_{k,4} \\ 0 & 0 & 0 & 0 & 0 \\ \vdots & \vdots & \vdots & \vdots & \vdots \\ 0 & 0 & 0 & 0 & 0 \end{bmatrix}. \quad (27)$$

For the disturbance state vector L_n , we use a model similar to what was already in use on the GRAVITY FT (see Paper 1), which gave satisfactory results, and which consists in a set of 6 Auto-Regressive (AR) models in OPD space (see Appendix A). Since the upgraded version of the FT is now using a state-model in OPL rather than in OPD space, this AR model needs to be converted to OPL space. To do so, we first note that for a 4-telescope (6-baseline) interferometer like GRAVITY, an OPD vector $\Phi = (\phi_{1,2}, \phi_{1,3}, \phi_{1,4}, \phi_{2,3}, \phi_{2,4}, \phi_{3,4})^T$ and an OPL vector $(l_1, l_2, l_3, l_4)^T$ are linked by the matrix equation:

$$\Phi = M \cdot l, \quad (28)$$

where M is a 6×4 matrix defined as:

$$M = \begin{bmatrix} 1 & -1 & 0 & 0 \\ 1 & 0 & -1 & 0 \\ 1 & 0 & 0 & -1 \\ 0 & 1 & -1 & 0 \\ 0 & 1 & 0 & -1 \\ 0 & 0 & 1 & -1 \end{bmatrix}. \quad (29)$$

Therefore, computing an OPL vector from knowledge of the OPD vector is under-constrained, yielding multiple solutions. A solution entails using the Moore-Penrose pseudo-inverse of M :

$$l = M^+ \cdot \Phi. \quad (30)$$

For reference, the value of M^+ is:

$$M^+ = \frac{1}{4} \begin{bmatrix} 1 & 1 & 1 & 0 & 0 & 0 \\ -1 & 0 & 0 & 1 & 1 & 0 \\ 0 & -1 & 0 & -1 & 0 & 1 \\ 0 & 0 & -1 & 0 & -1 & -1 \end{bmatrix}. \quad (31)$$

This particular choice ensures that the mean value of the OPLs on each telescope is 0, which is beneficial for a fringe-tracker. It helps avoid “runaway” situations where all the actuators move toward a large offset, saturating the system.

These equations can be extended to our OPL state-space vector L_n as defined in Equation 19, and a similarly defined OPD vector $\Phi_n = (\Phi_{n,1,2}, \dots, \Phi_{n,3,4})^T$ using similar matrices in which the “1s” are replaced by identity matrices of size 150:

$$\mathcal{M} = \begin{bmatrix} I_{150} & -I_{150} & 0 & 0 \\ I_{150} & 0 & -I_{150} & 0 \\ I_{150} & 0 & 0 & -I_{150} \\ 0 & I_{150} & -I_{150} & 0 \\ 0 & I_{150} & 0 & -I_{150} \\ 0 & 0 & I_{150} & -I_{150} \end{bmatrix}, \quad (32)$$

$$M^+ = \frac{1}{4} \begin{bmatrix} I_{150} & I_{150} & I_{150} & 0 & 0 & 0 \\ -I_{150} & 0 & 0 & I_{150} & I_{150} & 0 \\ 0 & -I_{150} & 0 & -I_{150} & 0 & I_{150} \\ 0 & 0 & -I_{150} & 0 & -I_{150} & -I_{150} \end{bmatrix}. \quad (33)$$

With these matrices, the relationships remain:

$$\Phi_n = \mathcal{M} \cdot L_n, \quad (34)$$

$$L_n = M^+ \cdot \Phi_n. \quad (35)$$

Our AR model fitting provides a set of 6 matrices $A_{j,k}$ which can be used to propagate the individual $\Phi_{n,j,k}$. These can be combined in a block-diagonal matrix to propagate Φ_n itself:

$$\Phi_{n+1} = \begin{bmatrix} A_{1,2} & 0 & \dots & 0 \\ 0 & A_{1,3} & \ddots & \vdots \\ \vdots & \ddots & \ddots & 0 \\ 0 & \dots & 0 & A_{3,4} \end{bmatrix} \cdot \Phi_n. \quad (36)$$

Switching to OPL space, we have:

$$\mathcal{M} \cdot L_{n+1} = \begin{bmatrix} A_{1,2} & 0 & \dots & 0 \\ 0 & A_{1,3} & \ddots & \vdots \\ \vdots & \ddots & \ddots & 0 \\ 0 & \dots & 0 & A_{3,4} \end{bmatrix} \cdot \mathcal{M} \cdot L_n. \quad (37)$$

At this point, we can note that:

$$\mathcal{M}^+ \cdot \mathcal{M} = I_{600} - \frac{1}{4} \begin{bmatrix} I_{150} & I_{150} & I_{150} & I_{150} \\ I_{150} & I_{150} & I_{150} & I_{150} \\ I_{150} & I_{150} & I_{150} & I_{150} \\ I_{150} & I_{150} & I_{150} & I_{150} \end{bmatrix}, \quad (38)$$

which means that as long as our OPL vectors L_{n+1} contain values where the average on all telescopes is 0, we can consider that $\mathcal{M} \cdot \mathcal{M}$ is the identity matrix. In other words, as long as:

$$\begin{bmatrix} I_{150} & I_{150} & I_{150} & I_{150} \\ I_{150} & I_{150} & I_{150} & I_{150} \\ I_{150} & I_{150} & I_{150} & I_{150} \\ I_{150} & I_{150} & I_{150} & I_{150} \end{bmatrix} \cdot L_{n+1} = 0, \quad (39)$$

we have:

$$\mathcal{M}^+ \cdot \mathcal{M} \cdot L_{n+1} = L_{n+1}. \quad (40)$$

Assuming temporarily that L_{n+1} fulfil the condition given by Equation 39, we can left-multiply Equation 37 by \mathcal{M}^+ to get:

$$L_{n+1} = \left(\mathcal{M}^+ \cdot \begin{bmatrix} A_{1,2} & 0 & \dots & 0 \\ 0 & A_{1,3} & \ddots & \vdots \\ \vdots & \ddots & \ddots & 0 \\ 0 & \dots & 0 & A_{3,4} \end{bmatrix} \cdot \mathcal{M} \right) \cdot L_n. \quad (41)$$

A block matrix multiplication inside the brackets gives the final form of our model in OPL state-space:

$$\hat{L}_{n+1} = A_L \cdot L_n, \quad (42)$$

with:

$$A_L = \begin{bmatrix} \frac{A_{1,2}+A_{1,3}+A_{1,4}}{4} & -A_{1,2}/4 & -A_{1,3}/4 & -A_{1,4}/4 \\ -A_{1,2}/4 & \frac{A_{1,2}+A_{2,3}+A_{2,4}}{4} & -A_{2,3}/4 & -A_{2,4}/4 \\ -A_{1,3}/4 & -A_{2,3}/4 & \frac{A_{1,3}+A_{2,3}+A_{3,4}}{4} & -A_{3,4}/4 \\ -A_{1,4}/4 & -A_{2,4}/4 & -A_{3,4}/4 & \frac{A_{1,4}+A_{2,4}+A_{3,4}}{4} \end{bmatrix}. \quad (43)$$

We can formulate two important remarks on the propagation model given by Equation 42. Firstly, since:

$$\begin{bmatrix} I_{150} & I_{150} & I_{150} & I_{150} \\ I_{150} & I_{150} & I_{150} & I_{150} \\ I_{150} & I_{150} & I_{150} & I_{150} \\ I_{150} & I_{150} & I_{150} & I_{150} \end{bmatrix} \cdot A_L = 0, \quad (44)$$

our propagation model always guarantees that the condition given by Equation 39 is fulfilled. Physically, this stems from the fact that our propagation model is really the conversion of an OPD model to OPL space, where we used the freedom given by the under-constrained nature of the conversion to explicitly guarantee that the average piston is always 0, through the definition of \mathcal{M}^+ in Equation 31. Secondly, the presence of \hat{L} with a ‘‘hat’’ in Equation 42 emphasises the fact that this is only a model-propagated estimate of L . There is no hat for X in Equation 23, since we consider our piezo model to be perfect (or at least much better than our atmospheric model).

Equation 42 is linear, and the covariance matrix on L_n is propagated accordingly, using an additional 600×600 matrix Q , which represents the ‘‘process noise’’.

$$\hat{P}_{n+1} = A_L \cdot P_n \cdot A_L^T + Q. \quad (45)$$

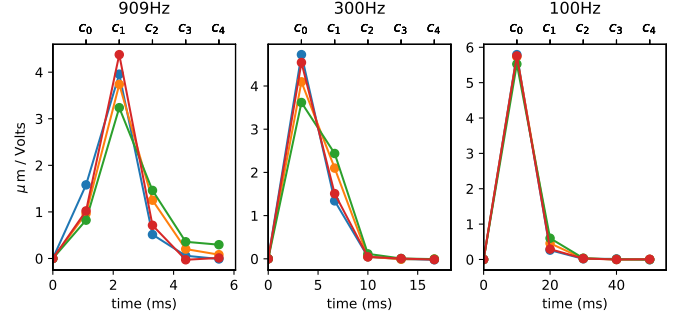


Fig. 1. Open loop response of the piezo control chain. This corresponds to the response of the piezo in micrometers per volt, as a function of time (bottom axis), when submitted to an impulse command. Equivalently, this also gives the values of the coefficients of the fifth order model used in Equation 20 (top axis). Each colour represents a distinct actuator.

The process noise Q is derived from a set of 150×150 matrices $Q_{j,k}$ using a similar block construction:

$$Q = \begin{bmatrix} \frac{Q_{1,2}+Q_{1,3}+Q_{1,4}}{4} & -Q_{1,2}/4 & -Q_{1,3}/4 & -Q_{1,4}/4 \\ -Q_{1,2}/4 & \frac{Q_{1,2}+Q_{2,3}+Q_{2,4}}{4} & -Q_{2,3}/4 & -Q_{2,4}/4 \\ -Q_{1,3}/4 & -Q_{2,3}/4 & \frac{Q_{1,3}+Q_{2,3}+Q_{3,4}}{4} & -Q_{3,4}/4 \\ -Q_{1,4}/4 & -Q_{2,4}/4 & -Q_{3,4}/4 & \frac{Q_{1,4}+Q_{2,4}+Q_{3,4}}{4} \end{bmatrix}. \quad (46)$$

The matrices $A_{j,k}$ and $Q_{j,k}$ are recalculated every 5 seconds by an asynchronous machine (`wgvkalm` described in sec 4.1) based on OPD measurements. This computation makes use of the Python toolbox ‘‘Time Series Analysis’’ (Seabold & Perktold 2010). A detailed explanation of its implementation is provided in Appendix A.

3.3. Phase control

Without any ‘‘feedback’’, i.e. any additional information about the state of the system, the internal model of the FT would simply keep propagating the state-vector L indefinitely using Equation 42, and dispatch commands to the piezo actuators to respond to its own predictions. This behaviour would probably be acceptable over a few iterations, but given the uncertainties on the predictions of the disturbance, the internal state-vector L_n would quickly diverge from the real values. The internal model is ‘‘aware’’ of this, as Equation 45 shows that in such a scenario, the covariance matrix would slowly inflate due to the accumulating ‘‘process noise’’ Q .

To properly track the fringes over long periods, the FT therefore needs to integrate measurements into the loop. But these measurements should not be taken at face value either, as they are also affected by varying levels of uncertainties. Integrating noisy measurements into the loop without careful consideration will create additional noise in the system, thereby reducing its overall performance. The main task of the Kalman controller in phase-delay loop is to determine how to best balance the information coming from the state model propagation, and from the additional measurements performed on the system. In Paper 1, this was done using a fixed asymptotic Kalman gain, which could not react in real time to the quality of the model and measurements. This new version of the Kalman provides an optimal gain, calculated at each iteration to combine the two sources of information in the best possible way.

At each time step t_n , we obtain a set of 6 measurements of the phase (or OPD) on each baseline, with an estimate of their

error bars. The measurement process is detailed in Section 2, and for the context of this Section, we will simply denote $\Phi_n = (\phi_{j,k}(t_n))$ the column vector of size 6 containing the individual phase measurements (see Equation 9), and W_n the associated 6×6 diagonal covariance matrix, as defined from Equation 15 in Equation 16.

These measurements are related to our state-vectors L_n and X_n through the ‘‘measurement equations’’:

$$\phi_{j,k}(t_n) = [l_k(t_n) - l_j(t_n) + x_k(t_n) - x_j(t_n)]_{\text{mod } \lambda_0}. \quad (47)$$

This means that although our state-vectors are of length 600 to accommodate for the group-delay measurements which are averaged over 150 DITs, the OPD measurement itself only relies on the first values (at time t_n) for each telescope. In matrix form, this can be written:

$$\Phi_n = [H_\phi \cdot (L_n + X_n)]_{\text{mod } \lambda_0}, \quad (48)$$

with H_ϕ defined by

$$H_\phi = \begin{bmatrix} v_1 & -v_1 & 0 & 0 \\ v_1 & 0 & -v_1 & 0 \\ v_1 & 0 & 0 & -v_1 \\ 0 & v_1 & -v_1 & 0 \\ 0 & v_1 & 0 & -v_1 \\ 0 & 0 & v_1 & -v_1 \end{bmatrix}, \quad (49)$$

where $v_1 = (1, 0, \dots, 0)^T$ is the first basis vector of length 150.

Given our assumption that the piezo state-vector X_n is perfectly known, the difference between the actual measurement and the expected measurement $\hat{\Phi}_n = H_\phi \cdot (\hat{L}_n + X_n)$ is directly related to the difference between the actual state of the disturbance L_n and its estimate \hat{L}_n :

$$\Phi_n - \hat{\Phi}_n = [H_\phi \cdot (L_n - \hat{L}_n)]_{\text{mod } \lambda_0} \quad (50)$$

and so, ignoring the modulo, it is tempting to simply update the state-vector according to $L_n = \hat{L}_n + H_\phi^+ \cdot (\Phi_n - \hat{\Phi}_n)$. But this would be reinjecting all the noise from the measurement into the control loop, without any consideration for the respective levels of confidence of the said measurement and the prediction from the model propagation.

These levels of confidence are represented by the matrices \hat{P}_n and W_n , which can therefore be used to calculate a Kalman gain which properly weights the model prediction and the measurement (Nowak 2019, section 4.3, for a proper derivation of this gain):

$$K_n = (\hat{P}_n \cdot H_\phi^T) \cdot (H_\phi \cdot \hat{P}_n \cdot H_\phi^T + W_n)^{-1}. \quad (51)$$

The update state-vector and its covariance matrix are then given by:

$$L_n = \hat{L}_n + K_n \cdot [\hat{\Phi}_n - \Phi_n + \Phi_{\text{CP},n}]_{\text{mod } \lambda_0}, \quad (52)$$

$$P_n = \hat{P}_n + K_n \cdot (H_\phi \cdot \hat{P}_n \cdot H_\phi^T + W_n) \cdot K_n^T, \quad (53)$$

which does indeed reduce to $L_n = \hat{L}_n + H_\phi^+ \cdot (\hat{\Phi}_n - \Phi_n + \Phi_{\text{CP},n})$ in the $W_n \ll \hat{P}_n$ regime, and also to $L_n = \hat{L}_n$ in the $\hat{P}_n \ll W_n$ regime.

The introduction of Φ_{CP} in this equation ensures a zero closure-phase on the measurement error. It is crucial to understand that the model being in OPL space, it cannot account for

any non-zero closure phase. This closure-phase issue was already present in the first version of the FT, and we refer to Section 4.2 of Paper 1 for a detailed explanation. We simply recall here that Φ_{CP} is constructed by setting three of the four closure phases $\theta_{j,k,l}^{\text{PD}}$ to the appropriate baselines, ignoring the closure phase on the triangle of lowest signal-to-noise ratio:

$$\Phi_{\text{CP}} = \begin{pmatrix} \theta_{1,2,4}^{\text{PD}} \\ \theta_{1,3,4}^{\text{PD}} \\ 0 \\ \theta_{2,3,4}^{\text{PD}} \\ 0 \\ 0 \end{pmatrix} \text{ or } \begin{pmatrix} \theta_{1,2,3}^{\text{PD}} \\ 0 \\ -\theta_{1,3,4}^{\text{PD}} \\ 0 \\ -\theta_{2,3,4}^{\text{PD}} \\ 0 \end{pmatrix} \text{ or } \begin{pmatrix} 0 \\ -\theta_{1,2,3}^{\text{PD}} \\ -\theta_{1,2,4}^{\text{PD}} \\ 0 \\ 0 \\ \theta_{2,3,4}^{\text{PD}} \end{pmatrix} \text{ or } \begin{pmatrix} 0 \\ 0 \\ 0 \\ \theta_{1,2,3}^{\text{PD}} \\ \theta_{1,2,4}^{\text{PD}} \\ \theta_{1,3,4}^{\text{PD}} \end{pmatrix}. \quad (54)$$

It is also important to note that given such a definition, two fundamentally different kinds of variations of Φ_{CP} can occur: (1) Φ_{CP} can change because of slowly varying closures phases in the measurements, in which case it is simply tracking actual variations; (2) Φ_{CP} can switch between options given in Equation 54, which occurs when the triangle of lowest signal to noise ratio changes. The second case corresponds to a change of configuration, leading to an abrupt variation of Φ_{CP} , and is therefore banned while the science detector is integrating. This behaviour is controlled thanks to an internal boolean parameter, called the mobility flag, which is ‘‘False’’ during science integrations.

3.4. Group delay control

The initial version of the FT described in Paper 1 was designed for an instrument performing prolonged exposures at a consistent wavelength of $2.2 \mu\text{m}$. As long as it stayed in the coherence envelope of the fringes, the FT had the freedom to transition from one fringe to another. This is unacceptable if the GRAVITY fringe tracker is to be used to feed a different science instrument operating at a different wavelength, as this would blur the fringes on the science detector. In an effort to make the GRAVITY FT compatible with the L-band combiner MATISSE (Lopez et al. 2022), the group delay controller has been modified to consistently track the same fringe during a scientific exposure. This new MATISSE mode is called GRA4MAT (Woillez et al. in prep.), and is now routinely offered to the community.

For this, the group delay control loop must determine in real time which fringe is being tracked by the phase-control loop, and updates the state-vector L_n by integer multiple of λ_0 if required, depending on which fringe it wants to track. Such changes are completely transparent to the phase control loop, due the modulo λ_0 in Equation (50).

To implement this behaviours, we use a formalism similar to the phase-delay loop. We first introduce the 6×600 measurement matrix H_ψ to relate the group-delay Ψ to the state-vectors L_n and X_n :

$$\Psi_n = H_\psi \cdot (L_n + X_n) \quad (55)$$

$$, \quad (56)$$

with

$$H_\psi = \frac{1}{150} \begin{bmatrix} \mathbf{1} & -\mathbf{1} & 0 & 0 \\ \mathbf{1} & 0 & -\mathbf{1} & 0 \\ \mathbf{1} & 0 & 0 & -\mathbf{1} \\ 0 & \mathbf{1} & -\mathbf{1} & 0 \\ 0 & \mathbf{1} & 0 & -\mathbf{1} \\ 0 & 0 & \mathbf{1} & -\mathbf{1} \end{bmatrix}, \quad (57)$$

and where $\mathbf{1} = (1, 1, \dots, 1)$ is a row-vector of length 150 full of “1s”. This is similar to the definition of H_ϕ , but includes an averaging of the past 150 DITs.

We also introduce Ψ_{CP} , an analogue of Φ_{CP} which is calculated using $\theta_{j,k,l}^{\text{GD}}$ instead of $\theta_{j,k,l}^{\text{PD}}$ in Equation 54, and an additional vector Ψ_{ZeroGD} . This additional setpoint is used to select which specific fringe will be set at a group delay of 0, to be tracked by the FT. Again, to avoid fringe jumps during a science integration, a mobility flag is used to freeze Ψ_{ZeroGD} during integrations on the science detector. When the mobility flag allows for changes, the Ψ_{ZeroGD} setpoint is estimated so that:

$$\left[\Psi_n - \hat{\Psi}_n - \Psi_{\text{CP}} - \Psi_{\text{ZeroGD}} \right]_{\text{mod } \lambda_0} = 0. \quad (58)$$

This condition is valid modulo λ_0 , which means that Equation 58 does not determine exactly which fringe will be tracked. To lift this uncertainty, two requirements must be added:

- R1: Vector Ψ_{ZeroGD} must be as small as possible.
R2: Vector Ψ_{ZeroGD} must not have a closure phase.

The first requirement is to ensure that the system is tracking the white light fringe. The second requirement is needed because the closure phase has already been nulled by the Psi_{CP} term.

Therefore, the zero group delay setpoint is estimated by the real time computer as:

$$\Psi_{\text{ZeroGD}} = M \cdot \left[M^\dagger \cdot (\Psi_n - \hat{\Psi}_n - \Psi_{\text{CP}}) \right]_{\text{mod } \lambda_0}, \quad (59)$$

where M was introduced in Equation 29, and M^\dagger is a pseudo inverse weighted by the covariance matrix W_n , i.e. the matrix that solves the linear system $Y = MX$ in the least-square sense, considering that W_n from by Equation 16 is the covariance matrix of X . This matrix M^\dagger can be calculated using:

$$M^\dagger = (M^T \cdot W_n \cdot M)^{-1} \cdot M^T \cdot W_n. \quad (60)$$

The controller ensures that the group delay never deviates by more than $\lambda_0/2$ from this setpoint. For this, the controller calculates at each cycle an error in the form of $\Psi - \hat{\Psi} - \Psi_{\text{CP}} - \Psi_{\text{ZeroGD}}$. It converts this group delay error to OPL space using M^\dagger from Equation 60. If this error exceeds $\lambda_0/2$ on any telescope, the controller subtracts λ_0 to all the 150 values corresponding to this telescope in the state-vector L . Similarly, if an OPL value falls below $-\lambda_0/2$, the elements of L corresponding to this telescope are increased by λ_0 . These adjustments by integer multiples of λ_0 never disturb the phase controller, due to the presence of a modulo λ_0 in Equation. 52, and thanks to the stationarity of the propagation model (more details in Appendix A).

3.5. Commands to the actuators

The command for the actuators is obtained from:

$$U_{n+1} = F \cdot L_n + U_{\text{setpoint},n} + U_{\text{search},n}. \quad (61)$$

In this equation, U_{setpoint} is used to modulate the position of the fringes, in a process detailed in Paper 1². This setpoint can now also be controlled externally by another machine – for example, to correct non-common optical path delays – as described in Section 4.1.

The term U_{search} is used to search for the fringes when they are lost by one or more telescopes. This is made to ensure that

² U_{setpoint} is called $U_{\text{modulation}}$ in Paper 1.

the FT continues to track the fringes on the baselines where they remain visible, while searching on the others.

The term $F \cdot L_n$ cancels out the disturbance calculated by the FT. More precisely, this term is used to negate the influence of the disturbance within a given number of “future” DITs. This number of DITs, d , is made to be adjusted to the mean response speed of the fringe tracker. Practically, it is $d = 2$ at 909 Hz, and $d = 1$ at lower frequencies. Hence, F is calculated such as:

$$C \cdot F \cdot L_n = H_\phi \cdot A^d \cdot L_n. \quad (62)$$

Which is obtained to the best of our capabilities, by taking:

$$F = \frac{1}{4} \begin{bmatrix} \frac{1}{C_{T1}} & \frac{1}{C_{T1}} & \frac{1}{C_{T1}} & 0 & 0 & 0 \\ \frac{-1}{C_{T2}} & 0 & 0 & \frac{1}{C_{T2}} & \frac{1}{C_{T2}} & 0 \\ 0 & \frac{-1}{C_{T3}} & 0 & \frac{-1}{C_{T3}} & 0 & \frac{1}{C_{T3}} \\ 0 & 0 & \frac{-1}{C_{T4}} & 0 & \frac{-1}{C_{T4}} & \frac{-1}{C_{T4}} \end{bmatrix} \cdot H_\phi \cdot A^d \quad (63)$$

with C_{T_k} representing the integrated impulse response of the piezo actuator at telescope k :

$$C_{T_k} = \sum_{n=0}^4 c_{k,n}, \quad (64)$$

where the c coefficients are the same as in Equation 20

3.6. Summary of the new control loop

The architecture of the new control loop is illustrated in Figure 2. As mentioned, in this updated architecture, the two control loops do not run in parallel anymore, as it was the case in Paper 1. To some extent, the phase loop can now be seen as the main control loop, and the group-delay control as an auxiliary loop which provides additional update of the state parameters to ensure proper tracking of the group delay. The phase tracking is done using a Kalman filter which does not rely on asymptotic gain anymore, but which uses a real-time covariance-weighted combination of a model prediction (in OPL space) and a measurement update (in OPD space). The control algorithm consists in the following steps:

1. At iteration n , we start with an estimate of the state-vector \hat{L}_n , propagated from the previous iteration. Our state-vector L contains the path length at each telescope over a given number $N = 150$ previous iterations. This estimate, which also comes with a covariance matrix \hat{P}_n , represents our best knowledge of the state parameters. We also have a state-vector X_n , which stores the position of the piezo actuators over the last 150 iterations.
2. From these state-vectors, we construct the total OPL at each telescope, which is simply $\hat{L}_n + X_n$, and then calculate the expected values for the phase and group delay ($\hat{\Phi}$ and $\hat{\Psi}_n$), using a set of “measurement” matrices H_ϕ and H_ψ , respectively given in Equations 49 and 57, and which convert our OPL-based vectors to our OPD-based measurements:
$$\hat{\Phi}_n = H_\phi \cdot (\hat{L}_n + X_n) \quad (65)$$

$$\hat{\Psi}_n = H_\psi \cdot (\hat{L}_n + X_n) \quad (66)$$
3. A measurement Φ of the OPDs is performed, which comes with an estimate of its uncertainties, in a process described in Section 2. The difference between this measurement and the expected value $\hat{\Phi}_n$ encodes some information on the state

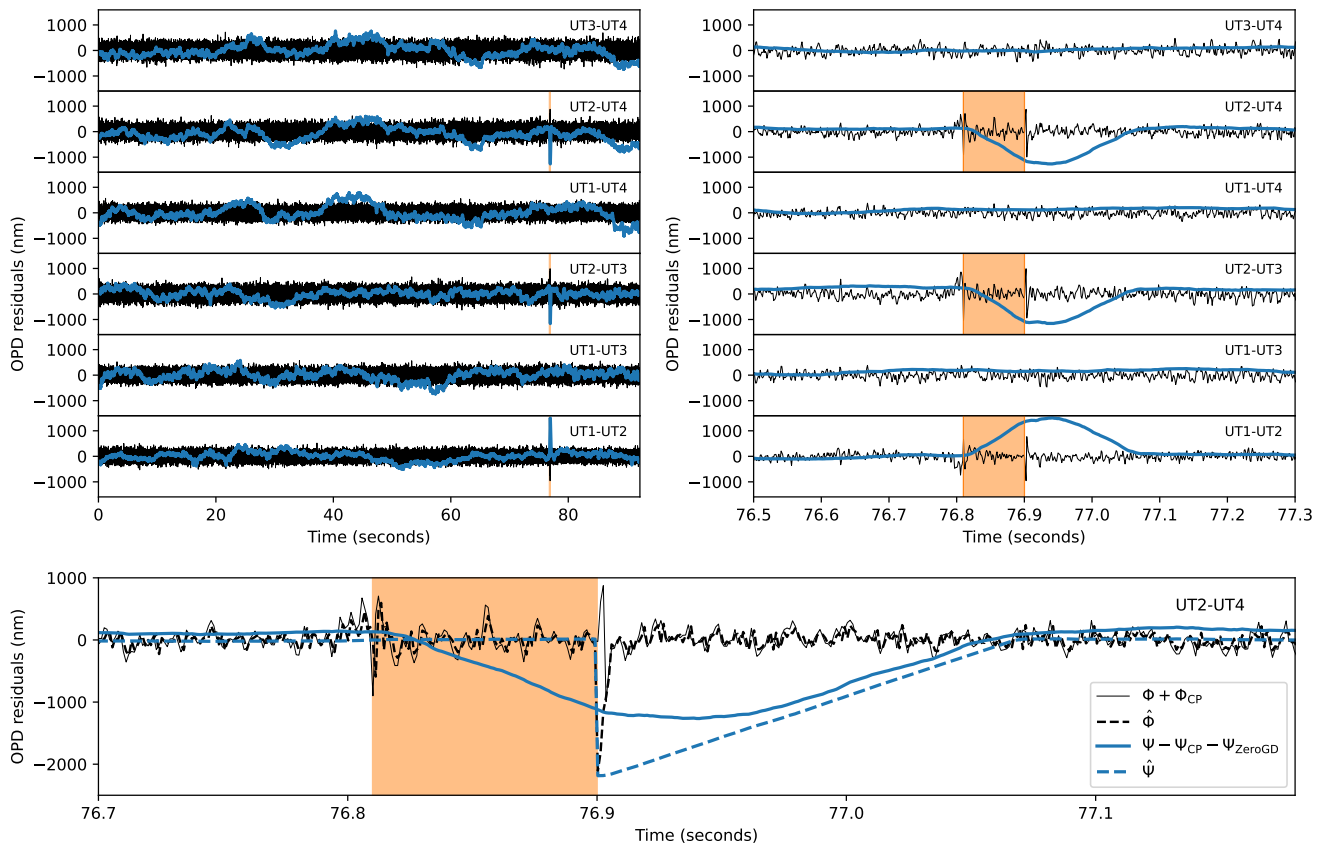


Fig. 4. Observation of star HR 8799 using GRAVITY. The data is from a single DIT exposure on the spectrometer, spanning 100 seconds. Black curves denote the OPD, derived from the phase delay: $(\Phi - \Phi_{CP})$. Blue curves illustrate observations from the group delay: $(\Psi - \Psi_{CP} - \Psi_{ZeroGD})$. Each panel represents a different baseline. At $t_1 = 76.81$ seconds, a noticeable fringe jump occurred on UT2. The effect of this jump across all baselines is depicted in the right panels. Impressively, the group delay identified and corrected the jump within 100 ms. The lower panel offers a magnified perspective of the baseline between UT2 and UT4, with overlaid predictions from the controller’s state: $\hat{\Phi}$ and $\hat{\Psi}$. Notably, at $t_2 = 76.9$ s, all predictions shifted by 2200 nm, marking the detection of the jump. To shift the OPD by one λ , the phase delay took 3 DITs (3.3 ms), while the group delay took 150 DITs (165 ms), attributed to the smoothing length of the observable.

is executed on dedicated cores, with a portion of the RAM isolated from the Linux kernel, ensuring efficient access by the Reflective Memory (PCIE-5565PIORC) via DMA (Direct Memory Access).

The Kalman filter parameters (A_L , Q , F) are recalculated every 5 seconds by another Linux workstation (`wgvkaln`). This workstation is also fitted with a PCIE Reflective Memory card, which allows it to record the OPDs calculated by `wgvfft` through the VLTI Reflective Memory Network (RMN) ring. This RMN ring is also used to transfer back the Kalman filter parameters to `wgvfft`.

An optional external machine, also connected to the RMN ring, can be used by another instrument to control the fringe tracker in real time. Such a workstation would have the possibility to send to `wgvfft` fringe tracking setpoints (the U_{setpoint}). It can also be used to send the mobility flag introduced after Equation 54.

The piston correction values calculated by the `wgvfft` workstation are transmitted to another workstation named `lgvttp`, using the RMN ring network. The `lgvttp` workstation operates with a Motorola CPU and is built around an mv6100 single-board computer, incorporating a VME bus for system communication. There, they are combined with external measurements of tip/tilt to form a comprehensive correction signal. This signal, in analog form, is then sent out to control four active mirrors

mounted on piezoelectric tip-tilt platforms provided by Physik Instrumente.

The commissioning of the updated hardware was conducted in late 2022, as part of the GRAVITY+ upgrade (Eisenhauer 2019; Gravity+ Collaboration et al. 2022), and was promptly made available to the scientific community. We could enable the white light fringe tracking a few months later, allowing the GRA4MAT mode of MATISSE (Wuillez et al. in prep.). Similarly, the new Kalman filter state model, introduced in June 2023, was immediately offered to the community upon commissioning.

4.2. Performance of the group-delay control loop: analysis of a fringe jump

On the 2nd of July 2023, we observed the exoplanet HR 8799 e during a scientific run of the ExoGRAVITY large programme (ESO LP 1104.C-0651). The atmospheric conditions were average, with a coherence time of 4 ms and a seeing of 0.8". The planet was at a separation of 440 mas, and we observed using the "off-axis dual-field" mode of the fringe tracker. We used the roof mirror to split the field, so that all the flux from the star was injected in the FT fibre, and all the flux of the planet in the science fibre.

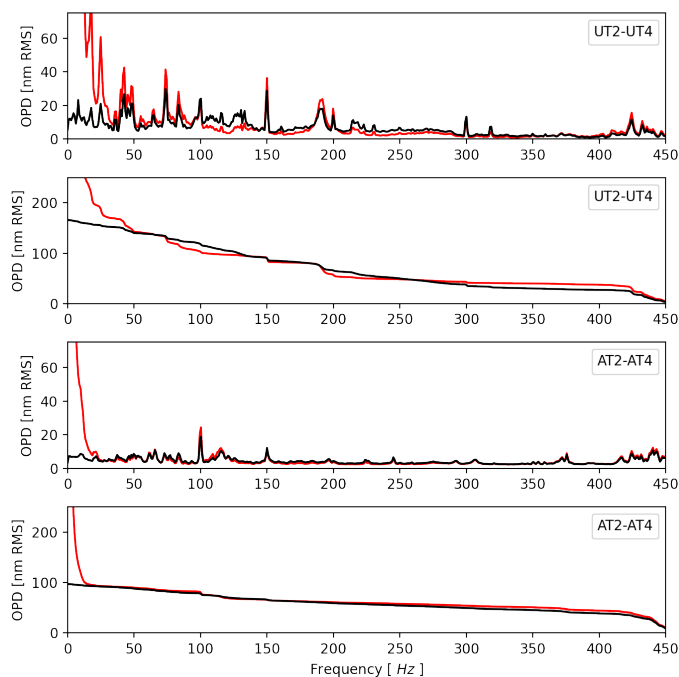


Fig. 5. Spectra of the residual OPD (shown in black) and the reconstructed perturbation ($H_\phi \cdot L$, depicted in red) for two observations. The upper panels present data on HR 8799 for one baseline from the Unit Telescopes (UTs) corresponding to the data showed in Figure 4. The standard deviation of OPD is 151 nm. The panel below showcases a dataset from the Auxilliary Telescopes (ATs) for HR 7672 with an OPD standard deviation of 86 nm. The cumulative spectrum for these 2 dataset are also showed. The data for all baselines are presented in Appendix. B.

Due to the faint nature of the exoplanets, these observations require extended integration times on the science channel, specifically DITs of 100 s in this example. To optimise contrast, the fringe tracker is instructed to remain on the same fringe for the entire 100 s duration. Figure 4 shows that the FT is able to properly track the fringes on all six baselines. The residual OPD of such a constant tracking is plotted in the upper left panel of Figure 4. HR 8799 is a bright star of magnitude 5.24 in K-band, and is not a challenging target for the fringe tracker, which easily tracks these fringes at an interferometric SNR of ~ 45 . The power spectrum of the OPD residuals is shown in Figure 5 and in Appendix. B.

Over a 100-second integration period, the phase-delay controller consistently tracks constant OPD values, maintaining a standard deviation of 150 nm in the residual OPDs. Intriguingly, the group-delay residuals are notably larger, yet they manifest at lower frequencies, showcasing variations over time scales of several seconds. The peak-to-peak amplitude of these variations remains under 1000 nm. As a result, the group-delay controller perceives no need for fringe adjustment, avoiding any false triggers for phase jump detection. Consequently, the phase-delay fringe tracker operates smoothly, successfully maintaining its tracking on the same phase.

Nonetheless, sporadic events can sometimes prompt the fringe tracker to transition abruptly from tracking one fringe to another, a full wavelength, λ_0 , apart. This phenomenon, unnoticed by the phase delay, is referred to as a ‘fringe jump’. A quintessential instance of this can be observed in Figure 4. This fringe jump manifested itself at $t_1 = 76.81$ seconds across all

baselines related to UT2. The lower panel of the figure gives the phase delay ($\Phi - \Phi_{CP}$), represented by solid black curves. This phase delay has already accounted for the closure phase vector, as outlined in Equation (10). A dashed black curve displays the estimation $\hat{\Phi}$ derived from the state parameters. Surrounding t_1 , the OPD shows fluctuations, but the Kalman filter overlooks the phase jump, and the λ_0 deviation in the OPD is not registered by $\hat{\Phi}$. This jump manifests itself in the group delay, represented by the solid blue curve in the figure. Owing to its smoothing over 150 DITs, the group delay gradually moves to a value close to $-\lambda/2$ at $t_2 = 76.9$. At this point, all the UT2-related OPL state-parameters of the phase control loop undergo a shift by λ_0 , induced by the group-delay controller. In the figure, this is evidenced by the abrupt λ_0 shift of both phase and group-delay state predictions ($\hat{\Phi}$ and $\hat{\Psi}$).

This example perfectly illustrates the behaviour of the group-delay controller, and shows that it required a span of 90 ms to detect the fringe jump. This interval represents the response time of the group delay control loop, and is dictated by the group delay’s smoothing length (the 150 DITs). This setting represents a balance between responsiveness and the potential for false positives due to noise³. As illustrated in the top right panels of Figure 4, predicting this noise is challenging as it does not appear to be purely random. The value of 150 retained in the algorithm has a mostly empirical basis.

4.3. Performance of the phase-delay control loop: OPD Residuals

In Paper 1, we discussed the OPD residuals observed in 2019, noting a significant dependence on the coherence time, τ_0 . During unfavourable conditions ($\tau_0 < 3$ mas), values typically exceeded 380 nm. Under average conditions ($3 \text{ mas} < \tau_0 < 7$ mas), these values ranged around 150 nm (ATs) or 250 nm (UTs), and under optimal conditions ($\tau_0 > 7$ mas), the UTs observed values down to 220 nm. We hypothesised that the inability of the UTs to reach residuals below 220 nm, even in the best atmospheric conditions, was due to vibrations.

Over the past four years, significant efforts have been made to mitigate these vibrations. Alongside the upgraded fringe-tracker, these efforts have resulted in notable improvements. Figure 5 display the spectrum of the OPD residuals for two targets, HR 8799 and HR 7672, over a single, representative, baseline. Description of the dataset and spectrum for all baselines are presented in Appendix B. The black solid curves represent the differential optical path measured by the fringe tracker (Φ), while the red curves depict the differential optical path reconstructed from the actuators: $\Phi + H_\phi \cdot X$.

For the UTs, vibrations are predominant, exhibiting significant components at high frequencies, such as 20 nm vibrations at 300 Hz and 40 nm at 150 Hz. The control system strives to cancel these out, achieving partial success. However, it inadvertently reintroduces noise at other frequencies, resulting in no substantial improvement in OPD residuals down to 50 Hz. This is evident in the cumulative spectrum, where the red and black curves exhibit similar amplitudes from 50 Hz upwards. Below 50 Hz, the fringe tracker is highly effective, cancelling even

³ In principle, this could be a tunable parameter, which could be adjusted on a per target basis. In the case of HR 8799, given the brightness of the star and the high interferometric SNR obtained, decreasing this value would likely result in better performances. However, in the framework in which the GRAVITY FT is implemented, this is a far from easy change to make, and this value remains currently fixed at 150 DITs.

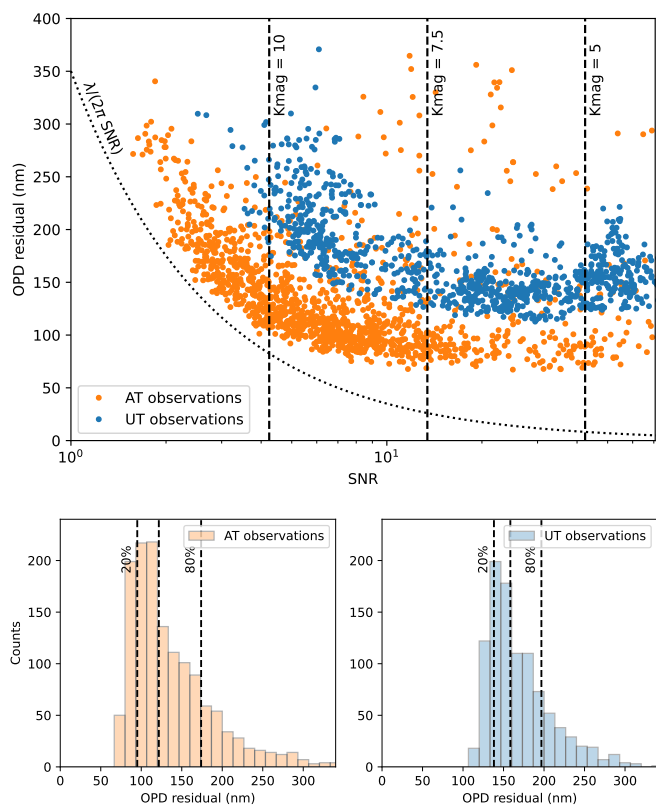


Fig. 6. OPD residuals. Top panel: OPD residuals plotted against the signal-to-noise ratio per baseline for all data collected from June to August 2023. The orange dots represent ATs observations, while the blue dots denote UTs observations. The dotted curve represents the theoretical limitation imposed by the measurement noise ($\lambda/2\pi\sigma_{j,k}$). The vertical dashed lines indicate the signal-to-noise ratio observed with the UTs of a star at a given star magnitude. It should be shifted by about 2.5 magnitude for the ATs. Bottom panels: histogram of the same OPD residuals as in the upper panel, for the ATs (left) and the UTs (right)

broad-frequency vibrations around 40 Hz. For the UTs, the most detrimental range is between 50 and 100 Hz, where a forest of spectral lines challenges the controller’s ability to correct them, contributing to the observed ≈ 150 nm of residual. Potentially, a faster response time in the control loop could further reduce residuals within this range.

On the ATs, vibrations are not the dominant factor in the residuals, which are characterised by a white noise pattern that aligns with the theoretically expected signal-to-noise ratio. For HR 7672, the dataset presented in Figure 5, the interferometric SNR is around 8, equating to a white noise level of 60 nm. Given that residuals for different baselines range between 71 and 93 nm, the system’s OPD residuals are close to the photon and background noise limitation. In this scenario, we observed the vibrations are minimal and do not degrade the interferometric SNR.

This behaviour of the ATs is also substantiated statistically, as demonstrated by the dataset present in the ESO archive on low signal datasets (SNR below 3). Figure 6 shows the OPD residuals for all calibrators observed from June to August 2023. To expand the dataset, additional observations within the ExoGRAVITY large program during this period are included. The upper panel of Figure 6 indicates that at lower fluxes for the ATs, the GRAVITY fringe tracker aligns closely with the theoretical phase error arising solely from noise, indicating a reach towards

the theoretical signal-to-noise limit. However, when the signal-to-noise ratio surpasses 3 for both UTs and ATs, the performance begins to diverge from this limit, potentially due to piston noise from external factors like the atmosphere.

In conclusion, the ATs’ residuals at the 20%, 50%, and 80% percentiles are 95 nm, 120 nm, and 170 nm (1σ), respectively, and for the UTs, the corresponding values are 135 nm, 150 nm, and 185 nm. These values are derived from the histograms in the lower panels of Figure 6. We observe a reduced dependence on the coherence time for performance, with optimal performance now achievable even at a low τ_0 of 2 ms.

5. Future Prospects

5.1. Areas of Improvement

There are at least three key areas that require further attention to enhance the capabilities of fringe tracking:

- Reducing OPD residuals at high SNR
- Enhancing signal-to-noise ratio for a given photon count
- Boosting sensitivity by operating at slower speeds

Regarding OPD residuals. The critical question is whether these can be further reduced at high signal-to-noise ratios. There appears to be potential for improvement on the UTs, as their performance, despite notable advances, still lags behind that of the ATs. Ignoring injection-related issues, the atmospheric piston impact on an 8 m telescope should in theory be less than on a 1.8 meter telescope (Conan et al. 1995). Given that the baselines in the astrometric configuration used in our AT observations of HR 7672 are very similar to the UT baselines, the fringe tracker should have achieved better results on the UTs, and reducing OPD residuals below 80 nm on the UTs should be feasible, with an ultimate atmospheric limitation of 5 nm according to Courtney-Barrer et al. (2022). The discrepancy in performance can be possibly attributed to instrumental vibrations, particularly high above 50 Hz (Figure 5), which the control loop struggle to correct, despite the fact that they seem to be properly captured by the model. Amplitude fluctuations induced by the performance of the Adaptive Optics (AO), with lower Strehl ratios observed on the UTs, are another major factor to take into account. A better control of the vibrations, as well as a better AO correction, will certainly help to further decrease the OPD residuals on the UTs.

Concerning signal-to-noise. Another question worthy of interest is whether the measured interferometric SNR matches the expectations given the magnitude of our targets. The observations of the bright target HR 8799 in July 2023 yielded an event rate of $n_{e^-/s/UT} = 10^7$ photons per telescope per second, suggesting a combined transmission for GRAVITY and VLTI of about 1%. The photometric SNR can be calculated as:

$$\text{SNR}_{\text{photometric}} = \sqrt{\frac{4n_{e^-/s/UT}\delta t}{\gamma}}. \quad (71)$$

where the factor 4 arises from the use of four telescopes, and γ represents the efficiency of the recombination architecture, with lower values being more desirable. At minimum, γ is inherently limited by the number of degrees of freedom in the system. Given the 16 degrees of freedom of our architecture (4 real fluxes and 6 complex coherent fluxes), an optimised beam combiner could theoretically achieve a γ as low as 16. Assuming $\gamma = 16$,

$\delta t = 0.00085^4$ and given the fact that the visibility is close to one for this unresolved target, the interferometric SNR for HR 8799 should be around 46, which indeed matches our measured value of ~ 45 . This implies that the γ value for GRAVITY is indeed close to 16, indicative of a well-designed combiner. Further improvements will require innovative approaches such as the Hierarchical Fringe Tracker could also potentially decrease the γ value by reducing the system's degrees of freedom (Petrov et al. 2022).

On ultimate sensitivity. During the June commissioning run, the exact sensitivity limit of the fringe tracker on the UTs remained undetermined, as the AO performance started to degrade at magnitudes below 10 (see UT data in Figure 6). The introduction of laser guide stars in GRAVITY+ is anticipated to extend the AO's limiting magnitude, potentially allowing us to ascertain the true sensitivity of the enhanced GRAVITY fringe tracker. Once the signal-to-noise ratio limit at 1 kHz is achieved, exploring a 100 Hz mode becomes a viable option for further boosting sensitivity by mitigating the detector's readout noise. In theory, as previously discussed, the theoretical atmospheric piston on an 8-meter telescope should be minimal, which could even enable operation as slow as 10 Hz. However, achieving this would necessitate a reduction in the instrumental piston caused by vibrations. Mechanical solutions, such as directly removing vibrations or compensating for them using accelerometers (as in the ongoing MANHATTAN-II project (Lieto et al. 2008; Woillez et al. 2018)), offer one approach. Alternatively, as these vibrations are intrinsic to the VLTI infrastructure, the optical path could be monitored and adjusted thanks to a dedicated metrology system, as proposed in the now-abandoned VibMET project (Woillez et al. 2018).

5.2. Unexplored possibilities

Using the GRAVITY fringe tracker alongside other instruments introduces a number of challenges in maintaining fringe tracking accuracy across different wavelengths. At a basic level, this requires the fringe tracker to avoid "fringe jumps", a critical improvement implemented by the new algorithm described in this paper. But a notable observation also pertains to the issue of varying atmospheric dispersion. The blue curves in Figure 4 display slowly changing dispersion patterns. While the GD smoothing is approximately 150 ms, the blue curves exhibit correlations over significantly longer durations, up to 10 s. This can be attributed to fluctuations in water vapour, as investigated in the works of Colavita et al. (2013) and Müller et al. (2014). Such signals hold relevance for infrared instruments, such as ELT/METIS (Absil et al. 2022), but could also be addressed at the fringe tracker level to adjust the setpoint, ensuring stable fringes at another wavelength despite the changing dispersion.

Machine learning algorithms represent another unexplored avenue in the realm of fringe-tracking. These algorithms have the potential to integrate a broader spectrum of information compared to our current Kalman filter-based loop. Data from AO wavefront sensors and/or telescope vibration sensors, for instance, could substantially enhance fringe-tracking capabilities (Perera et al. 2022). A model, trained on a comprehensive dataset, could leverage this additional information for more accurate performance. The success observed in Adaptive Optics, particularly with reinforcement learning (Pou et al. 2022), hints

at the potential advancements that machine learning could bring to fringe tracking.

6. Conclusion

In this work, we have introduced a new approach to fringe tracking, based on a Kalman filter working in OPL state-space. This state-space is non-observable, which makes the integration of measurements trickier than when working in OPD space. In particular, this leads to a somewhat cumbersome transformation of the AR model used to predict the evolution of the OPD disturbances to OPL space. But the rewards is a reduction of dimensionality of the state-space, from 6 (the number of baselines, or OPDs) to 4 (the number of telescopes, or OPLs). In the case of the new GRAVITY FT, this allows us to propagate covariance-matrices on the state-vector, and hence to use an optimal Kalman gain, dynamically calculated at each iteration.

We described this new algorithm specifically in the context of GRAVITY, but the conceptual framework can be seamlessly extended to various other instruments. As opposed to the number of OPDs, which grows quadratically with the number of telescopes in the array, the number of OPLs only grows linearly. Therefore, the gain offered by this novel approach increases with the size of the array, thereby offering a compelling solution for future concepts such as the Planet Formation Imager (Monnier et al. 2018).

In the meantime, with this new version of the GRAVITY fringe tracker, ESO is now able to offer the interferometric community a facility fringe tracker that not only delivers competitive performance but also ensures seamless integration within the VLTI environment. This new fringe tracker is already in use with MATISSE (the GRA4MAT mode, described in Woillez et al. in prep.). Beyond this, it could also accommodate visitor instruments, becoming a useful tool for a much larger community.

Acknowledgements. The authors wish to express their gratitude to the anonymous referee for an excellent report, which contained both useful suggestions to improve the paper, corrections of important mistakes, and ideas for future work. GRAVITY was developed in a collaboration of the Max Planck Institute for Extraterrestrial Physics, LESIA of Paris Observatory, IPAG of Université Grenoble Alpes / CNRS, the Max Planck Institute for Astronomy, the University of Cologne, the Centro Multidisciplinar de Astrofísica from Lisbon and Porto, and the European Southern Observatory. This work used observations collected at the European Southern Observatory under ESO programme 1104.C-0651 and 109.238N.003. SL, JBL, and FM acknowledge the support of the French Agence Nationale de la Recherche (ANR), under grant ANR-21-CE31-0017 (project ExoVLTI). DD and RL have received funding from the European Research Council (ERC) under the European Union's Horizon 2020 research and innovation program (grant agreement CoG - 866070). PG acknowledges the financial support provided by FCT/Portugal through grants PTDC/FIS-AST/7002/2020 and UIDB/00099/2020. SL would like to warmly thank Sylvain Rousseau for spotting many typographical errors in the equations of Paper 1.

References

- Absil, O., Delacroix, C., Orban de Xivry, G., et al. 2022, in Society of Photo-Optical Instrumentation Engineers (SPIE) Conference Series, Vol. 12185, Adaptive Optics Systems VIII, ed. L. Schreiber, D. Schmidt, & E. Vernet, 1218511
- Abuter, R., Dembet, R., Lacour, S., et al. 2016, in Society of Photo-Optical Instrumentation Engineers (SPIE) Conference Series, Vol. 9907, Optical and Infrared Interferometry and Imaging V, ed. F. Malbet, M. J. Creech-Eakman, & P. G. Tuthill, 990721
- Cassaing, F., Le Duigou, J.-M., Houairi, K., et al. 2008, in Optical and Infrared Interferometry, ed. W. C. Danchi, F. Delplancke, & M. Schöller, Vol. 7013, Proc. Soc. Photo-Opt. Instrum. Eng.
- Choquet, É., Menu, J., Perrin, G., et al. 2014, A&A, 569, A2
- Colavita, M. M., Booth, A. J., Garcia-Gathright, J. I., et al. 2010, PASP, 122, 795
- Colavita, M. M., Wizinowich, P. L., Akeson, R. L., et al. 2013, PASP, 125, 1226

⁴ The discrepancy between this integration time and the running frequency of 909 Hz is explained by the detector readout and reset time.

- Conan, J. M., Rousset, G., & Madec, P.-Y. 1995, *Journal of the Optical Society of America A*, 12, 1559
- Courtney-Barrer, B., Woillez, J., Laugier, R., et al. 2022, in *Society of Photo-Optical Instrumentation Engineers (SPIE) Conference Series*, Vol. 12183, *Optical and Infrared Interferometry and Imaging VIII*, ed. A. Mérand, S. Sallum, & J. Sanchez-Bermudez, 1218328
- Delplancke, F., Derie, F., Lévêque, S., et al. 2006, in *Proc. SPIE*, Vol. 6268, *Society of Photo-Optical Instrumentation Engineers (SPIE) Conference Series*, 62680U
- Eisenhauer, F. 2019, in *The Very Large Telescope in 2030 (Astronomy Australia Ltd)*
- Eisenhauer, F., Monnier, J. D., & Pfuhl, O. 2023, *ARA&A*, 61, 237
- Finger, G., Baker, I., Alvarez, D., et al. 2014, in *Society of Photo-Optical Instrumentation Engineers (SPIE) Conference Series*, Vol. 9148, *Adaptive Optics Systems IV*, ed. E. Marchetti, L. M. Close, & J.-P. Vran, 914817
- GRAVITY Collaboration, Abuter, R., Aymar, N., et al. 2022, *A&A*, 657, L12
- Gravity+ Collaboration, Abuter, R., Alarcon, P., et al. 2022, *The Messenger*, 189, 17
- GRAVITY Collaboration, Abuter, R., Amorim, A., et al. 2018a, *A&A*, 615, L15
- GRAVITY Collaboration, Abuter, R., Amorim, A., et al. 2020a, *A&A*, 636, L5
- GRAVITY Collaboration, Abuter, R., Amorim, A., et al. 2018b, *A&A*, 618, L10
- GRAVITY Collaboration, Abuter, R., Amorim, A., et al. 2019a, *A&A*, 625, L10
- GRAVITY Collaboration, Abuter, R., Amorim, A., et al. 2021, *A&A*, 647, A59
- GRAVITY Collaboration, Amorim, A., Bauböck, M., et al. 2020b, *A&A*, 643, A154
- GRAVITY Collaboration, Bauböck, M., Dexter, J., et al. 2020c, *A&A*, 635, A143
- GRAVITY Collaboration, Dexter, J., Shangguan, J., et al. 2020d, *A&A*, 635, A92
- GRAVITY Collaboration, Lacour, S., Nowak, M., et al. 2019b, *A&A*, 623, L11
- GRAVITY Collaboration, Nowak, M., Lacour, S., et al. 2020e, *A&A*, 633, A110
- GRAVITY Collaboration, Perraut, K., Labadie, L., et al. 2019c, *A&A*, 632, A53
- GRAVITY Collaboration, Pfuhl, O., Davies, R., et al. 2020f, *A&A*, 634, A1
- GRAVITY Collaboration, Sturm, E., Dexter, J., et al. 2018c, *Nature*, 563, 657
- Houairi, K., Cassaing, F., Perrin, G., et al. 2008, in *Optical and Infrared Interferometry*, ed. W. C. Danchi, F. Delplancke, & M. Schöller, Vol. 7013, *Proc. Soc. Photo-Opt. Instrum. Eng.*
- Lacour, S., Dembet, R., Abuter, R., et al. 2019, *A&A*, 624, A99
- Lacour, S., Jocu, L., Moulin, T., et al. 2008, in *Proc. SPIE*, Vol. 7013, *Optical and Infrared Interferometry*, 701316
- Le Bouquin, J.-B., Bauvir, B., Haguenaer, P., et al. 2008, *A&A*, 481, 553
- Lieto, N., Haguenaer, P., Sahlmann, J., & Vasisht, G. 2008, 7013
- Lopez, B., Lagarde, S., Petrov, R. G., et al. 2022, *A&A*, 659, A192
- Lozi, J., Cassaing, F., Le Duigou, J.-M., et al. 2011, in *Techniques and Instrumentation for Detection of Exoplanets V*, ed. S. Shaklan, Vol. 8151, *Proc. Soc. Photo-Opt. Instrum. Eng.*
- Menu, J., Perrin, G., Choquet, E., & Lacour, S. 2012, *A&A*, 541, A81
- Monnier, J. D., Kraus, S., Ireland, M. J., et al. 2018, *Experimental Astronomy*, 46, 517
- Müller, A., Pott, J. U., Mérand, A., et al. 2014, *A&A*, 567, A98
- Nowak, M. 2019, *Theses*, Université Paris sciences et lettres
- Perera, S., Pott, J.-U., Woillez, J., et al. 2022, *MNRAS*, 511, 5709
- Petrov, R. G., Allouche, F., Boskri, A., et al. 2022, in *Society of Photo-Optical Instrumentation Engineers (SPIE) Conference Series*, Vol. 12183, *Optical and Infrared Interferometry and Imaging VIII*, ed. A. Mérand, S. Sallum, & J. Sanchez-Bermudez, 121830I
- Petrov, R. G., Malbet, F., Weigelt, G., et al. 2007, *A&A*, 464, 1
- Pfuhl, O., Haug, M., Eisenhauer, F., et al. 2014, in *Proc. SPIE*, Vol. 9146, *Optical and Infrared Interferometry IV*, 914623
- Pou, B., Ferreira, F., Quinones, E., Gratadour, D., & Martin, M. 2022, *Optics Express*, 30, 2991
- Quirk, M. & Liu, B. 1983, in *ICASSP '83. IEEE International Conference on Acoustics, Speech, and Signal Processing*, Vol. 8, 1095–1098
- Seabold, S. & Perktold, J. 2010, in *9th Python in Science Conference*
- Shao, M., Colavita, M. M., Hines, B. E., et al. 1988, *Astronomy and Astrophysics*, 193, 357
- Sorrente, B., Cassaing, F., Rousset, G., RobbeDubois, S., & Rabbia, Y. 2001, *Astronomy & Astrophysics*, 365, 301
- Tary, J. B., Herrera, R. H., & van der Baan, M. 2014, *Geophysical Journal International*, 196, 600
- Tatulli, E., Millour, F., Chelli, A., et al. 2007, *A&A*, 464, 29
- Woillez, J., Abuter, R., & et al. in prep., *A&A*
- Woillez, J., Darré, P., Egner, S., et al. 2018, in *Society of Photo-Optical Instrumentation Engineers (SPIE) Conference Series*, Vol. 10701, *Optical and Infrared Interferometry and Imaging VI*, ed. M. J. Creech-Eakman, P. G. Tuthill, & A. Mérand, 1070103
-
- ¹ Institute of Astronomy, University of Cambridge, Madingley Road, Cambridge CB3 0HA, United Kingdom
e-mail: mcn35@cam.ac.uk
- ² Kavli Institute for Cosmology, University of Cambridge, Madingley Road, Cambridge CB3 0HA, United Kingdom
- ³ LESIA, Observatoire de Paris, Université PSL, CNRS, Sorbonne Université, Univ. Paris Diderot, Sorbonne Paris Cité, 5 place Jules Janssen, 92195 Meudon, France
- ⁴ European Southern Observatory, Karl-Schwarzschild-Straße 2, 85748 Garching, Germany
- ⁵ Max Planck Institute for extraterrestrial Physics, Giessenbachstraße 1, 85748 Garching, Germany
- ⁶ Research School of Astronomy & Astrophysics, Australian National University, ACT 2611, Australia
- ⁷ Department of Physics & Astronomy, University of Southampton, Hampshire, SO17 1BJ, Southampton, UK
- ⁸ Max Planck Institute for Astronomy, Königstuhl 17, 69117 Heidelberg, Germany
- ⁹ Univ. Grenoble Alpes, CNRS, IPAG, 38000 Grenoble, France
- ¹⁰ Institute of Astronomy, KU Leuven, Celestijnenlaan 200D, B-3001 Leuven, Belgium
- ¹¹ Laboratoire Lagrange, Observatoire de la Côte d’Azur, CNRS, Boulevard de l’Observatoire, CS 34229, 06304 Nice, France
- ¹² Université de Lyon, CNRS, Centre de Recherche Astrophysique de Lyon UMR 5574, 69230 Saint-Genis-Laval, France
- ¹³ Universidade do Porto, Faculdade de Engenharia, Rua Dr. Roberto Frias, 4200-465 Porto, Portugal
- ¹⁴ CENTRA - Centro de Astrofísica e Gravitação, IST, Universidade de Lisboa, 1049-001 Lisboa, Portugal
- ¹⁵ 1. Institute of Physics, University of Cologne, Zùlpicher Straße 77, 50937 Cologne, Germany

Appendix A: Determination of the propagation matrix $A_{j,k}$ and process noise $Q_{j,k}$

The goal of this appendix is to derive the $A_{j,k}$ and $Q_{j,k}$ representing the AR models in OPD space, and used in Equation 43 and 46. Both $A_{j,k}$ and $Q_{j,k}$ matrices are obtained using the `statsmodels` Python library (Seabold & Perktold 2010) from a sequence of 10,000 Φ_n vectors (≈ 10 s at 909 Hz). The challenge in estimating the propagation matrix lies in its need to be resilient to unwrapping errors. It should also not produce aberrant values in situations where the fringes are undetected or lost.

To address this, the matrices are determined based on phase differences rather than the phases themselves. Explicitly, for each baseline, we compute $\Delta\phi_{j,k,n} = [\phi_{j,k,n} - \phi_{j,k,n-1}]_{\text{mod } \lambda_0}$. To ensure reliable default operation during low signal-to-noise ratios on this baseline (e.g., when fringes are absent or lost), we set $\Delta\phi_{j,k,n} = 0$.

The `statsmodels`'s time series analysis is then employed to fit an AR model to the 9,999 $\Delta\phi_{j,k,n}$ values, one baseline at a time. We use the `statsmodels.tsa.ar_model.AutoReg` class to fit an AR model of order 22 using conditional maximum likelihood. The AR(22) model was chosen as it strikes a balance between computational efficiency and its ability to fit low frequencies. With 22 samples at 909 Hz, the minimum frequency and resolution of the predictor can be expected to be around 40 Hz. In practice, though, we find that the resolution is much better, and we are able to fit for frequencies as low as ~ 10 Hz, in line with the fact that AR models are notoriously better in terms of resolution than Fourier-Transform based algorithm (Quirk & Liu 1983; Tary et al. 2014).

The `statsmodels.tsa.ar_model.AutoReg` class fit gives six vectors of 22 values for the AR model, $g_{l,j,k}$, along with six scale parameters $q_{l,j,k}$. The AR(22) model of the phase difference is then integrated to give an AR(23) model g' of the phase itself, using:

$$g'_{0,j,k} = g_{0,j,k}, \quad (\text{A.1})$$

$$g'_{23,j,k} = -g_{22,j,k}, \quad (\text{A.2})$$

$$g'_{l,j,k} = g_{l,j,k} - g_{l-1,j,k} \quad \text{for } l \text{ between 1 and 22.} \quad (\text{A.3})$$

This ensures the stationarity of our model since $\sum_{l=0}^{23} g'_{l,j,k} = 0$. The propagation matrices representing the AR model are then:

$$A_{j,k} = \begin{bmatrix} g'_{0,j,k} & g'_{1,j,k} & \cdots & g'_{21,j,k} & g'_{22,j,k} & 0 & \cdots & 0 \\ 1 & 0 & \cdots & 0 & 0 & 0 & \cdots & 0 \\ 0 & 1 & 0 & \cdots & 0 & 0 & \cdots & 0 \\ 0 & 0 & 1 & \cdots & 0 & 0 & \cdots & 0 \\ \vdots & \vdots & \vdots & \ddots & \vdots & \vdots & \vdots & \vdots \\ 0 & 0 & 0 & \cdots & 1 & 0 & \cdots & 0 \\ 0 & 0 & 0 & \cdots & 0 & 1 & 0 & 0 \\ 0 & 0 & 0 & \cdots & 0 & 0 & 1 & 0 \end{bmatrix}, \quad (\text{A.4})$$

These matrices are of dimension 150×150 , but only the first 23 values and the sub-diagonal are non-zero. The AR(23) could be represented by a 23×23 matrix, but the extra-dimensions are required by our state-space model, which also needs to account for the group-delay.

The matrix $Q_{j,k}$ is also of dimension 150×150 . It is more straightforwardly generated from the scale parameter $q_{0,j,k}$ which correspond to the variance of the residuals in the `statsmodels`

fit:

$$Q_{j,k} = \begin{bmatrix} q_{0,j,k} & 0 & \cdots & 0 \\ 0 & 0 & \cdots & 0 \\ \vdots & \vdots & \ddots & \vdots \\ 0 & \cdots & \cdots & 0 \end{bmatrix} \quad (\text{A.5})$$

Appendix B: Power spectrum density

In Figures B.1 and B.2, we present the Fourier transforms of 100 seconds of fringe tracking OPD, Φ , acquired with the UTs and the ATs, respectively. The first dataset was obtained using the UTs to observe HR 8799 ($K_{\text{mag}} = 5.44$) on July 2, with an effective K magnitude of 4.4. The second dataset was captured using the ATs, in the "astrometric" configuration (A0-G1-J2-K0) to observe HR 7672 ($K_{\text{mag}} = 4.4$) on July 21. The exact file IDs for these observations are "GRAVI.2023-07-02T09:52:22.630" and "GRAVI.2023-07-21T06:16:19.030". Atmospheric conditions were good during the HR 8799 observations with a seeing of 0.8" and wind speed of 3.9 to 4.6 m/s, and excellent during the HR 7672 observations with a seeing of 0.4" and wind speed of ~ 2.8 m/s. We used Welch's method from the `scipy` library to compute the spectrum and cumulative spectrum of the OPD. The overall standard deviations of the OPDs are provided in the figure captions.

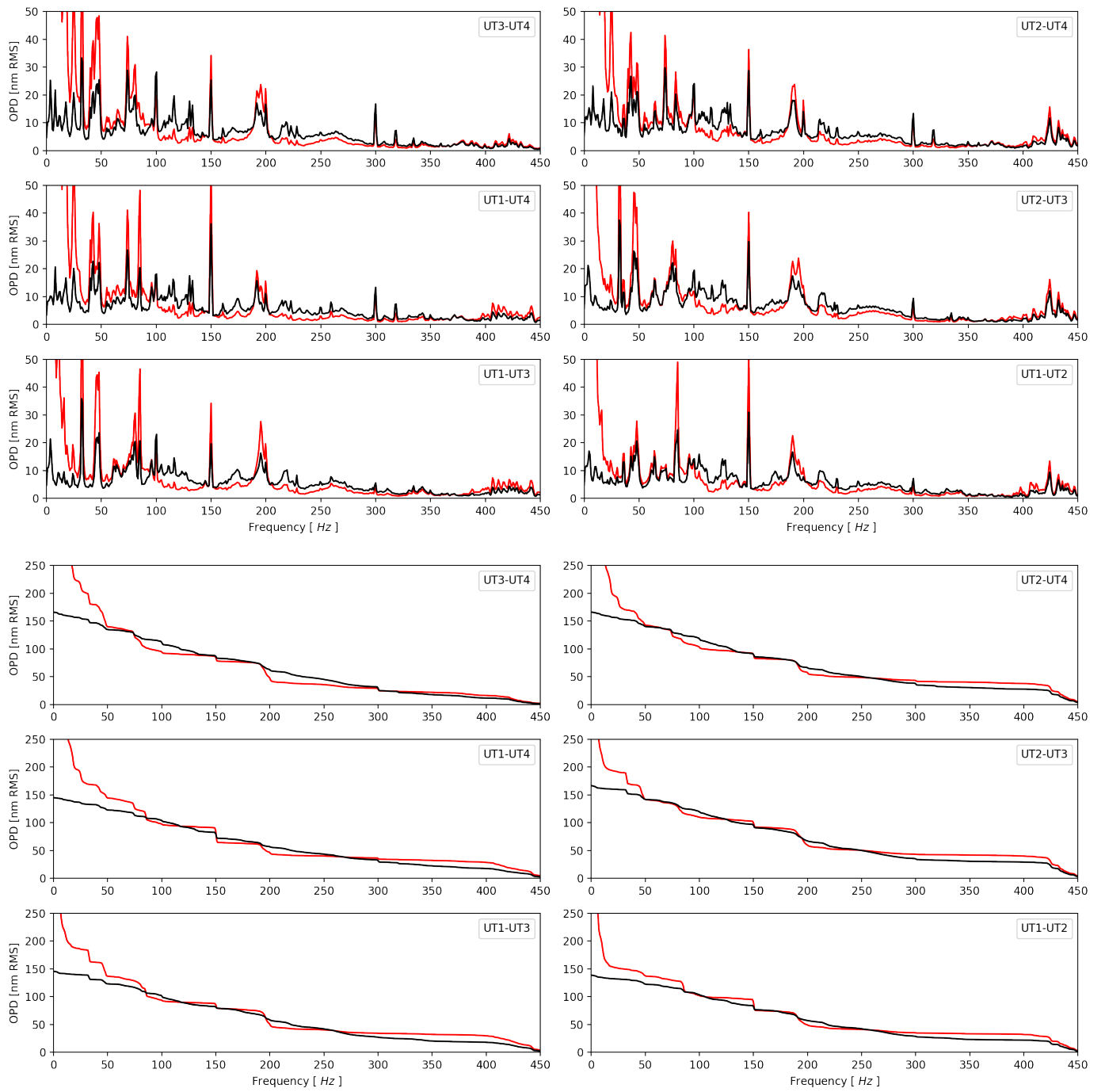


Fig. B.1. Power spectrum density (PSD) and cumulative sum of the PSD of phase residuals (Φ_n) for target HR 8799. The red curves represent the pseudo open-loop values, signifying the scenario without a fringe tracker ($H_\phi \cdot L$). The six lower plots show the reverse cumulative sum of the power spectrum. Over 100 s of a single scientific DIT, the residual standard deviation is 158 nm (UT3-UT4), 150 nm (UT2-UT4), 133 nm (UT1-UT4), 152 nm (UT2-UT3), 138 nm (UT1-UT3) and 124 nm (UT1-UT2).

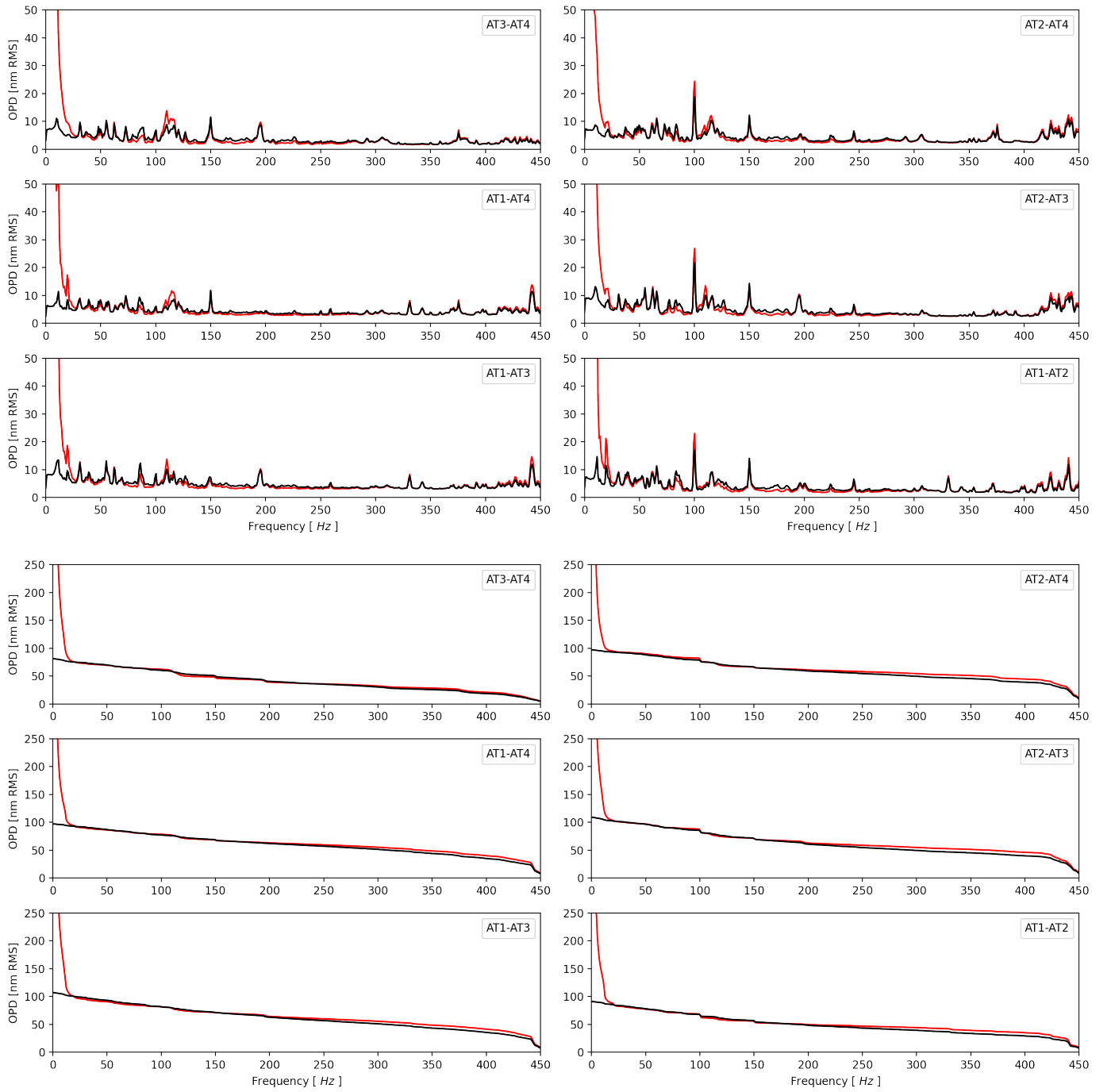


Fig. B.2. Power spectrum density (PSD) and cumulative sum of the PSD of phase residuals (Φ_n) for target HR 7672. The red curves represent the pseudo open-loop values, signifying the scenario without a fringe tracker ($H_\phi \cdot L$). The six lower plots show the reverse cumulative sum of the power spectrum. Over 100 s of a single scientific DIT, the residual standard deviation is 71 nm (UT3-UT4), 86 nm (AT2-AT4), 86 nm (AT1-AT4), 93 nm (AT2-AT3), 93 nm (AT1-AT3) and 80 nm (AT1-AT2).